PHYSICAL REVIEW B **67**, 214202 (2003)

# Structure and electronic properties of a nongraphitic disordered carbon system and its heat-treatment effects

Kazuyuki Takai,* Meigo Oga, Hirohiko Sato, and Toshiaki Enoki
*Department of Chemistry, Tokyo Institute of Technology, Ookayama, Meguro, Tokyo, 152-8551, Japan*

Yoshimasa Ohki[†] and Akira Taomoto[‡]
*Matsushita Electric Industrial Co., Ltd., Higashimita, Tama-ku, Kawasaki, 214-8501, Japan*

Kazutomo Suenaga and Sumio Iijima
*Japan Science and Technology Corporation, Department of Material Science and Engineering, Meijo University, Tenpaku-ku, Nagoya 468-8502, Japan*

(Received 9 November 2001; revised manuscript received 21 January 2003; published 19 June 2003)

The heat-treatment effect on electronic properties is investigated in relation to structural change for pulsed-laser-deposited amorphous carbon thin films having $sp^2/sp^3$ ratio $\approx 9$. The heat treatment at temperatures 200–400 °C increases conductivity and modifies the hopping conduction mechanism at low temperatures, resulting in the generation of a Coulomb gap at $E_F$. This is attributed to the heat-treatment-induced modification of the disorder nature of the structure from atomic-scale $sp^2/sp^3$ disorder to a disordered graphitic $sp^2$-domain network by the migration of $sp^3$ defects. In the heat-treatment temperature region above 600 °C, where the structure is featured with graphitic $sp^2$ domains, considerably small positive thermoelectric power is suggestive of carrier compensation by the competition of hole and electron carriers that originate from the inhomogeneous charge distribution caused by the difference of Fermi levels among graphitic $sp^2$ domains. In the high-heat-treatment-temperature region 800–1100 °C, the formation of an infinite percolation path network of the graphitic $sp^2$ domains induces an insulator-to-metal transition, where the electron transport in the $sp^2$-rich metallic state is featured by weakly temperature-dependent conductivity with majority hole and minority electron carriers.

DOI: 10.1103/PhysRevB.67.214202 PACS number(s): 71.23.Cq, 63.50.+x, 72.15.Jf, 72.20.Jv

## I. INTRODUCTION

Diamond and graphite are representative allotropes of carbon, which are formed with tetrahedral $sp^3$ and hexagonal $sp^2$ bond networks, respectively. Interestingly, there is a definite difference in the electronic structures between the two allotropes; that is, diamond is an insulator with an energy gap of 5.3 eV between $\sigma$ and $\sigma^*$ bands, while the presence of $\pi$ and $\pi^*$ bands around the Fermi energy $E_F$, which fill the $\sigma$-$\sigma^*$ gap, makes graphite semimetallic as described by the two-dimensional (2D) $\pi$-electron system.[1] Graphite is the equilibrium phase of carbon in the ambient condition.

Between the two allotropes, which are considered as extremes, disordered carbons having arbitrary $sp^2/sp^3$ bond concentration ratios are spread in a wide spectrum. At the same time, disordered carbon systems with the same $sp^2/sp^3$ ratio show a variety of different electronic structures owing to the clustering features of $sp^2$ carbons.[2] In the case with majority $sp^2$ carbons, the degree of clustering of $sp^2$ carbons is a particularly significant factor on the electronic properties of disordered carbon systems. By adding randomness to the graphitic structure with the $sp^2$-site distribution being inhomogeneous in space, "graphitic" disordered carbon systems are produced, where the microscopic structure is described as a random assembly of nanosized graphitic $sp^2$-carbon domains (nanographites). Many of works have been carried out in such graphitic disordered carbon systems from both experimental[3–5] and theoretical[6,7] aspects on the correlation between the structure and electronic properties.

On the other hand, the homogeneous distribution of $sp^2$ sites (also $sp^3$ sites) in $sp^2/sp^3$ mixture completely destroys the graphitic structure and makes conjugated $\pi$-electron structure disappear, even if the $sp^3$concentration is comparatively small. The structural model based on the assembly of graphitic domains is no longer adequate. "Nongraphitic" disordered carbon systems thus produced correspond to the state of carbon at high temperature and/or high pressure far from ambient state, and they appear as the metastable state of carbon in ambient condition. Many structural investigations have been reported on nongraphitic disordered carbons having various structural forms and $sp^2/sp^3$ ratios: diamondlike carbon (DLC),[8–12] tetrahedral carbon (ta-C),[11,13–17] glassy carbon.[18,19] However, only a few experimental works were reported on their electronic properties,[17,20] although theoretical works predicted anomalousness in their electronic features, different from the graphitic disordered state. Tight-binding and *ab initio* calculations claim uniqueness in the electronic structure inherited to nongraphitic $sp^2/sp^3$ mixture.[21,22] Namely, $sp^3$ sites in $sp^2/sp^3$ -mixed clusters mainly govern the generation of a large gap, which is almost in the same range as that of diamond ($\sim$5 eV), while pairs, even-membered rings, and chains of $sp^2$-carbon atoms form $\pi$-like states with a smaller gap ($\sim$2 eV). In contrast, isolated $sp^2$ sites and odd-membered rings of $sp^2$-carbon atoms give localized states in the gap. Thus, a finite density of states around $E_F$ is suggested for the disordered carbon systems in spite of the absence of graphitic structure. It is intriguing to investigate what electronic structure comes about in the absence of the graphitic $\pi$ electrons in $sp^2$-rich disordered carbon systems from the experimental view point.

In the present paper, we discuss the electronic properties of $sp^2$-rich, but nongraphitic, disordered carbon, in relation to heat-treatment-induced structural change. Samples were prepared by the heat treatment of nongraphitic carbon films prepared by pulsed laser deposition as starting material, which consists of a majority of $sp^2$ sites and a minority but a significant amount of $sp^3$ sites. Sample structural characterization was carried out by x-ray diffraction (XRD), electron energy loss spectroscopy (EELS), scanning electron microscopy (SEM), and Raman spectroscopy. The electronic properties were examined by means of dc electrical conductivity and thermoelectric power.

## II. EXPERIMENT

Samples were prepared by pulsed laser deposition method by a Q-switched Nd:YAG pulse laser (Spectron laser systems SL802G) with a highly oriented pyrolytic-graphite (HOPG) target in a vacuum chamber. The chamber was evacuated with a turbo-molecular pump to a base pressure of typically $2\times10^{-5}$ Torr prior to deposition. With the base pressure and chamber volume, the residual gas amount is calculated as $5.3\times10^{-9}$ mol. Even if the entire amount was incorporated into the sample, the content of hydrogen or oxygen in the sample became only about 1% with the assumption that the residual gas had the same composition as that of air. The laser wavelength, pulse width, and repetition rate were fixed at 532 nm, 4 ns, and 10 Hz, respectively. The laser power density and diameter of the laser beam were 0.14 W/mm$^2$ and 3.2 mm at the target surface, respectively. The sample films were deposited on quartz glass substrates placed 40 mm apart from the target with a mask having a size of $4\times6$ mm. The substrate temperature, the irradiation time, and the sample thickness measured by the needle probe method were typically 23 °C, 5 min, and 1 $\mu$m, respectively. The prepared samples were exfoliated from the quartz substrate by using a razor blade and organic solvent (ethanol or acetone) before structural characterization, electronic measurements and heat treatment.

The samples were heat treated in different ways depending upon the heat-treatment temperature (HTT) range. For heat treatment below 1100 °C, the samples were heat treated in a Pyrex or quartz tube by an electric furnace for 30 min in vacuum under $1\times10^{-6}$ Torr, while in the range 1300–1500 °C, the samples vacuum sealed under a pressure of $1\times10^{-6}$ Torr in a quartz tube in advance were heat treated. For convenience, the samples heat treated at xx00 °C will be labeled ‘‘HTT xx00’’ and the non-heat-treated sample is labeled ‘‘non-HT’’ hereafter.

SEM measurements were carried out by using a Hitachi S-800 field-emission-type microscope with acceleration voltage of 20 kV under $1\times10^{-6}$ Torr.

XRD measurements were carried out using synchrotron radiation (40 kV, 50 mA, 1.0027 Å, High Energy Accelerator Research Organization-Photon Factory) and a MacScience Micro Powder Diffractometer with cylindrical imaging plate detector and graphite monochromator. The wavelength of the incident light was calibrated based on the lattice constant of cerium oxide as a reference.

EELS spectra were measured by using a Gatan Imaging Spectrometer (GIF200) attached to JEOL2010F transmission electron microscope at an acceleration voltage of 200 kV under $1\times10^{-7}$ Torr in the energy loss range 0–305 eV. The convergence angle $\beta$ of the incident beam and the energy resolution were typically around 10 mrad and 1 eV, respectively.

Raman spectroscopy measurements were performed by using Jobin-Yvon T64000 spectrometer with an argon-ion laser operated at 514.5 nm with an output power of 10–30 mW in the backscattering geometry and a multichannel CCD counter in the wave number range 800–1900 cm$^{-1}$.

Electrical conductivity measurements were carried out for a single film with a voltage applied parallel to the film in the temperature range from 4.2 K to room temperature under 15 Torr helium exchange gas. Because of the high resistivity of the samples, the two-contact method was adopted for the measurements of the non-HT and HTT 200, while samples heat treated above 400 °C, which had low resistivity, were measured by the four-contact method. The samples were mounted on a copper pattern on a glass-epoxy resin substrate and electrically contacted with carbon paste.

Thermoelectric power measurements were performed using a single film along the film surface direction, where the ordinary two-probe method was used in the temperature range from 4.2 K to room temperature. Because of the high resistivity, it was impossible to measure thermoelectric power for the non-HT samples. Two 0.07% AuFe-Chromel (AuFe-Ch) thermocouples, whose absolute thermoelectric power had been calibrated in advance using pure lead (99.999%),[23] were contacted to the two ends of the sample using carbon paste. A coiled 50-Ω manganium wire was attached to one of the contact points as a heater, and a temperature gradient of about 0.3–1 K was made between the contacts. The thermoelectric powers of circuits AuFe-sample-AuFe (output voltage $V_{\mathrm{AuFe}}$) and Ch-sample-Ch (output voltage $V_{\mathrm{Ch}}$) were measured with two nanovoltmeters synchronized by a trigger from the electrical source of the heater. Thus, the thermoelectric power of the sample $S$ was obtained as follows:

$$S=\frac{V_{\mathrm{Ch}}S_{\mathrm{AuFe}}-V_{\mathrm{AuFe}}S_{\mathrm{Ch}}}{V_{\mathrm{Ch}}-V_{\mathrm{AuFe}}}, \tag{1}$$

where $S_{\mathrm{AuFe}}$ and $S_{\mathrm{Ch}}$ are the absolute thermoelectric powers of AuFe and Ch wires, respectively. The temperature of the sample was measured using platinum and germanium resistance thermometers placed near the sample.

## III. RESULTS

The non-HT samples appear brittle and blackish with metallic luster, being suggested to have a significant amount of $sp^2$-carbon bonds. SEM observation with a magnification of

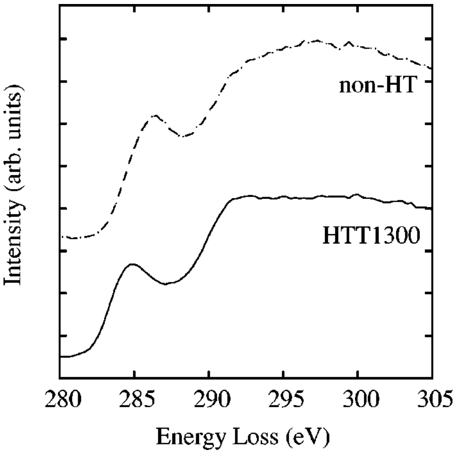

FIG. 1. *K*-edge spectra (single-scattering distributions) for non-HT and HTT 1300. The base lines of the spectra are shifted vertically from each other for clarify.

10 000× showed very smooth and nonporous nature of the sample surface.

Figure 1 shows the *K*-edge spectra for non-HT and HTT 1300. The spectra shown are single-scattering distributions extracted using the Fourier-ratio method.[24] Compared with the spectra for diamond and graphite, the peak around 285 eV is attributed to the $\pi$-$\pi^*$ transition of $sp^2$ carbon, while the large broad area between 290 and 300 eV mainly originates from the $\sigma$-$\sigma^*$ transitions of $sp^2$ and $sp^3$carbons.[25] Thus, the $sp^2/sp^3$ ratio of the samples is estimated from the ratio of the integrated intensities of the two peaks.[25] The $sp^2/sp^3$ ratios of both non-HT and HTT 1300 are calculated as $\sim 9$, suggesting that the sample are in the $sp^2$-rich region. Therefore, the EELS spectra for the present samples claim the fact that $sp^2/sp^3$ ratio ~ca. 9 is not changed by the heat treatment up to 1300 °C.

The XRD profile depends on the alignment of samples with respect to the direction of the incident x-ray beam as shown in Fig. 2. In either case with an incident x-ray beam between parallel and perpendicular to the sample film plane, the absence of any peak in the XRD pattern suggests that the samples for HTT$\lesssim$400 °C do not have any regularity in their structure even in the atomic-scale range. Thus, these samples have the disorder nature with jumbling of $sp^2/sp^3$ carbon atoms in the atomic scale. The diffraction peaks assigned to graphitic structure [(002), (004), and (006) for the beam direction parallel to the film plane and (100)/(101) for that perpendicular to the film direction] appear in the range HTT>600 °C, accompanied by the increase of their peak intensity and the decrease of their peak linewidth upon the elevation of HTT. This suggests that graphitic structure becomes important in the local structure upon the elevation of HTT. Interestingly, the temperature range, in which the structural change toward graphitic structure occurs, is considerably lowered in comparison with the typical graphitization temperature (~1600 °C).[1] This proves that, in the non-HT sample, the $sp^2/sp^3$ mixed structure having atomic-scale disorder with 10% $sp^3$ sites is in a nonequilibrium state far from a thermodynamically stable state and tends to be easily relaxed to graphitic state which is thermodynamically well defined, consistent with previous works.[18,26]

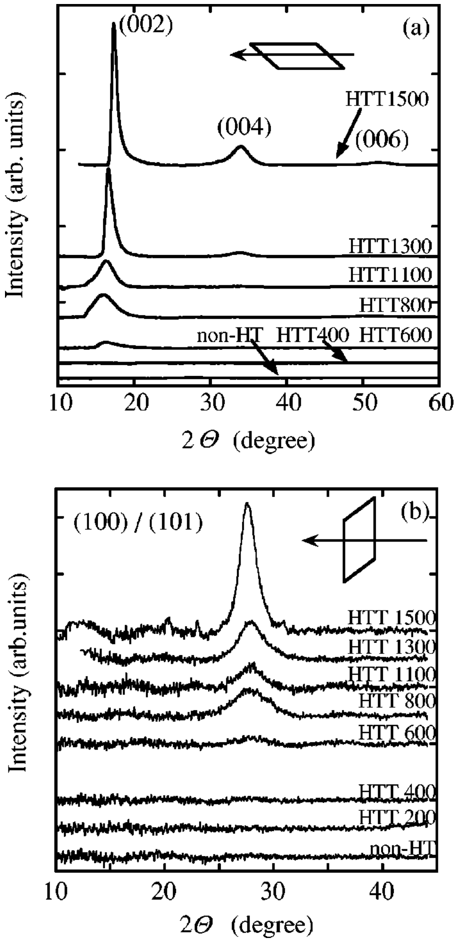

FIG. 2. (a) XRD patterns of the samples at various HTT's, where the film plane is aligned parallel to the incident x-ray beam. The indices of the Bragg reflections are shown for graphite (002), (004), and (006). (b) XRD patterns of the samples at various HTT's, where the film plane is aligned perpendicular to the incident x-ray beam. The graphite (100)/(101) Bragg reflection appears for HTT>600 °C. The base lines of the patterns are shifted vertically from each other for clarify. The schematical views of the film samples are illustrated with the incident x-ray beam direction.

XRD can add information on the orientation and shape of growing graphitic domains in the samples. In the case of sample film alignment with its plane parallel to the incident x-ray beam [Fig. 2(a)], a graphite (002) peak appears around 17° in the region of HTT>600 °C. In contrast, in the film alignment with its plane perpendicular to the incident x-ray beam [Fig. 2(b)], the (002) peak is not noticeable, while the peak around 28° assigned to graphite (100)/(101) emerges in this alignment. Peak (002) is related to the graphite stacking structure, while peaks (100)/(101) are associated with the in-plane structure. Judging from the observed anisotropic growth of these two kinds of XRD peaks shown in Fig. 2, graphite hexagonal sheets develop with the stacking direction perpendicular to the sample thin layer upon heat treatment even in the early stage of heat treatment (HTT ~600 °C). Such anisotropic growth of the graphite stacking structure in thin-layer disordered carbon systems was also

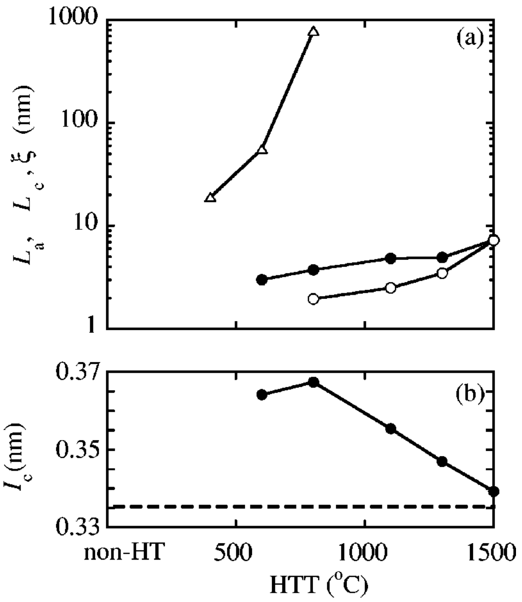

FIG. 3. (a) The HTT dependence of the in-plane size $L_a$ and the *c*-axis thickness $L_c$ of graphitic domain. $L_a$ is estimated from XRD (100)/(101) peak (solid circles), while $L_c$ is estimated from the XRD (002) peak (open circles). The localization length $\xi$ estimated from the conductivity is also shown as open triangles. (b) The HTT dependence of the interlayer distance $I_c$ of graphitic structure for the samples calculated from the XRD (002) peak position. Dashed line denotes the value for bulk regular graphite.

reported in ion-implanted glassy carbon,[18,19] ta-C,[17] and thermally annealed ta-C,[16] where the in-plane strain of the thin layer is important for the preferable direction of the growth of graphite stacking structure. A similar mechanism can be proposed in the case of the present non-HT samples, where the nonequilibrium carbon deposition process generates a large strain with respect to the in-plane direction.

The in-plane size ($L_a$) and *c*-axis thickness ($L_c$) of graphitic domains are obtained from the linewidths of the (100)/(101) and (002) peaks, respectively. The dimension of $L_a$ is calculated from the following relation obtained in consideration of 2D lattice diffraction:[27]

$$L_a = \frac{1.84\lambda}{B_{1/2}(2\Theta)\cos\Theta}, \tag{2}$$

where $\lambda$ and $B_{1/2}(2\Theta)$ are the wavelength of the x-ray beam and the full width at half maximum in radian units, respectively. The *c*-axis thickness $L_c$ is obtained by using the ordinary Scherrer formula[1]

$$L_c = \frac{0.89\lambda}{B_{1/2}(2\Theta)\cos\Theta}. \tag{3}$$

The estimated $L_a$ and $L_c$ from the XRD linewidths are shown in Fig. 3(a). As clearly seen in Fig. 3(a), the evolution of the graphitic domains is anisotropic between the in-plane and *c*-axis directions. In the in-plane direction, the graphitic hexagonal structure starts developing at HTT 600, at which the graphitic domains have a mean in-plane size of $\sim 3$ nm. Graphitization proceeds almost monotonically with the elevation of HTT. In contrast, the graphitic stacking structure starts growing from $L_c \sim 2$ nm at HTT 800, which tracks the development of the in-plane structure coherence. It becomes rapidly developing above about HTT 1100, and the $L_c$ values reach $\sim 7$ nm at HTT 1500, which is almost the same as that of $L_a$ at the same HTT. Namely, the graphitic domains in the samples have a thin flat-faced shape below HTT 1100, while they have an almost isotropic-block-like shape in the region HTT$>$1100 °C.

Generally speaking with chemical consideration, the conversion from the $sp^3$carbon to the $sp^2$ one takes place above $\sim$1200 °C.[28] Moreover, the $sp^2/sp^3$ ratio ($\sim 9$) of the present samples estimated from the EELS does not change so much for HTT$<$1300 °C. Therefore, the presence of a large anisotropy in the structure indicates that a sort of anisotropic local structure dominated by $sp^2$-coordinated carbon sites exists even in the non-HT sample, which can be easily transformed to the planar hexagonal graphitic network structure with plane orientation parallel to the in-plane direction of the sample thin layer, without any $sp^2/sp^3$ conversion. This can be understood on the basis of a homogeneous spatial distribution of $sp^3$ defects in a 2D hexagonal $sp^2$-carbon network in the non-HT sample. A carbon atom at an $sp^3$-defect site on an $sp^2$-hexagonal plane is considered to be cross-linked to an $sp^3$carbon on the adjacent hexagonal network plane. The presence of an $sp^3$ site on the graphitic plane depresses the conjugate $\pi$ character of three neighbor rings. Therefore, it is easily understood that the conjugated $\pi$ system almost disappears in the whole plane, when $sp^3$ defects are homogeneously distributed at 10% $sp^3$-defect concentration. In other words, even 10% $sp^3$ defects can contribute to the complete destruction of the hexagonal $\pi$-conjugated network, resulting in nongraphitic carbon structures. This leads to the disappearance of the graphitic diffraction peak in the low HTT samples. Local distortion due to $sp^3$ defects considerably enhances the lattice energy in the $sp^2$-carbon network, generating the metastable feature of the non-HT sample. These $sp^3$ defects can migrate upon heat treatment in the $sp^2$-carbon network by exchanging bonds with a low-energy barrier. Therefore, even small thermal energy can induce the relaxation to graphitic structure from the metastable structure of the non-HT sample, the former of which is the thermodynamically equilibrium state of carbon in an ambient condition. In this process, the cross-link defects migrate so as to form graphitic domains for minimizing the lattice distortion energy. Similar structural change by the migration of minority $sp^2$ sites was reported also in the $sp^3$-rich disordered carbon system.[15] It is considered that a large concentration of $sp^2$ sites in the present sample contributes to make $sp^3$ sites migrate easily resulting in the condensation of $sp^2$ sites. In the high-temperature range above HTT$\sim$1300 °C, the conversion from $sp^3$carbon to $sp^2$carbon starts and graphitization proceeds similarly to other disordered carbons.

Figure 3(b) shows the HTT dependence of the interlayer distance $I_c$ of the graphitic structure for samples calculated from the XRD (002) peak position. When the graphitic structure starts developing at HTT$\sim$600, the interlayer distance is $I_c = 0.364$ nm, which is considerably larger than that

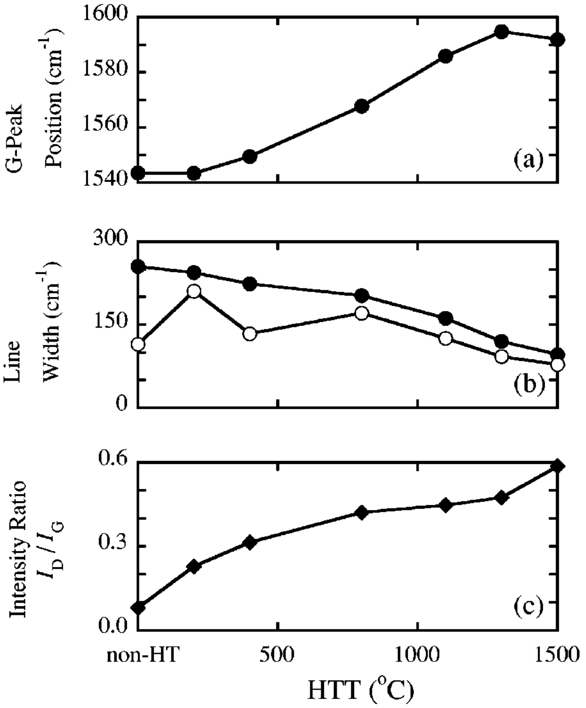

FIG. 4. The peak position (a), the linewidth (b), and the integrated peak intensity ratio of the *D* peak to *G* peak (c) of Raman spectra for the samples at various HTTs. Solid circles and open circles in (b) denote the linewidths of the *G* and *D* peaks, respectively. The solid lines are guides for the eyes.

of bulk graphite ($I_c = 0.3354$ nm). As HTT increases above 800 °C, it monotonically decreases and reaches almost the value for bulk regular graphite above HTT 1500. The peak has an asymmetric shape with a steep low-angle tail in HTT 600, 1300, and 1500, which suggests that the interlayer distances of graphitic structure in the HTT sample are distributed with larger contributions from larger interlayer distances. In the less graphitized region (HTT$\sim$600 °C), the contribution of $sp^3$ defects scattered on hexagonal graphitic sheets is expected to expand the interlayer distance due to the formation of cross-links between sheets and local lattice deformations, even if the $sp^3$-site concentration is in the range of 10%. Larger graphitic domains tend to give smaller interlayer distances since flat hexagonal graphitic sheet can easily make a dense packing in comparison with a defective sheets having poor flatness. Therefore, the asymmetric diffraction peak shape demonstrates that the size distribution of graphite domains is rather narrow with large domains less contributing. It should be noted that the HTT 1500 sample still has an appreciable contribution of $sp^3$ defects, taking into account that the interlayer distance is larger than that of bulk regular graphite.

The presence of cross-link $sp^3$ defects also affects the lattice dynamics of the sample, as evidenced by the Raman spectra of the low HTT samples, which are far from those of bulk regular graphite. In graphitic disordered systems, which are stabilized in the $sp^2$-rich state, well-defined graphitic domains are considered to be homogeneously distributed in general. In this case, the Raman feature is composed of two broad peaks around 1360 cm$^{-1}$ and 1590 cm$^{-1}$, which are assigned to the *D*-band peak and the Raman-allowed $E_{2g_2}$ mode (*G* band) in the general first-order features, respectively.[1] In fact, the Raman spectra for the samples in the region HTT>400 °C exhibit *G* and *D* peaks. However, the feature of the Raman spectra is much modified in the low HTT region (HTT$\lesssim$400 °C); a significant downshift of the *G* peak and the obscurity of the *D*-peak feature. Namely, they give a single broad asymmetric peak with a tail on the low-wave-number side, which has been typically observed in nongraphitic $sp^2/sp^3$-mixed carbons in the literature.[12,14,17,18] This indicates that the structure in that region is far from a disordered graphitic lattice, consistent with the results of XRD.

The spectra are fitted with the Breit-Fano-Wagner (BWF) line for the *G*-band peak and a Lorentzian for the *D*-band peak with the peak position, the linewidth, and the BWF coupling coefficient as adjustable parameters. Figure 4 shows the HTT dependence of the peak position, the linewidth, and the integrated peak intensity ratio of the *D* peak to the *G* peak in the Raman spectra. The *G* peak is located at 1544 cm$^{-1}$ for the non-HT samples, and it is gradually shifted up as HTT increases. In the region HTT>1100 °C, it almost reaches the value of the *G*-peak position of ordinary graphitic disordered carbon ($\sim$1590 cm$^{-1}$).[1] The linewidth of the *G* peak decreases monotonically from 256 cm$^{-1}$ for the non-HT samples and it reaches 96 cm$^{-1}$ for the HTT 1500. The intensity ratio of the *D* peak to *G* peak increases from 0.08 at non-HT as HTT increases, and it reaches 0.59 at HTT 1500. In the case of the ideal crystalline system, only the phonon modes satisfying the crystal momentum conservation rule can contribute to the Raman spectra. In fact, the Raman spectra for bulk regular graphite have only a single peak at 1585 cm$^{-1}$, although the phonon density of states (PDOS) of graphite has an intense peak around 1600 cm$^{-1}$. However, for the highly disordered systems (atomic scale disorder), in which the non-HT and low HTT samples were involved, all phonon modes contribute to the Raman spectrum, because the crystal momentum is no longer conserved. Therefore, the Raman spectrum almost reflects the PDOS, where peaks in the density of states dominate the peak profile in the spectrum. In the low HTT region, the $sp^3$ defects introduced into the hexagonal $sp^2$ layer distort sixfold rings, and such bond-angle disorder and bond bending cause its phonon modes to soften, particularly for the *G* band. Here, the PDOS deviates far from that of graphite, and the *D* band (breathing mode of $A_{1g}$ symmetry), which is strictly connected to the presence of sixfold-"ordered" $sp^2$ rings, disappears. Upon the development of graphitic structure with heat treatment, the PDOS tends to take that of graphite. Then, the *D* band corresponding to the aromatic ring character grows up, and the *G* peak is upshifted toward that of graphite. Note that even for the samples with higher HTT, the crystal momentum conservation is not enough, and the prohibited phonon modes in the *G* band still contribute to the spectra. Therefore, the contribution of the large density in the graphitic PDOS around 1600 cm$^{-1}$ induces a *G* peak with a higher position than that of graphite for HTT 1300. In HTT 1500, the *G* peak shifts down again, because the contribution

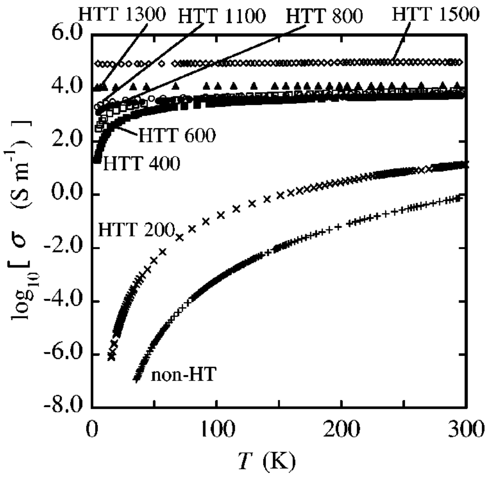

FIG. 5. The temperature dependence of the electrical conductivity $\sigma$ of the samples at various HTTs. Pluses, crosses, solid squares, open squares, solid circles, open circles, triangles, and diamonds denote non-HT, HTT 200, 400, 600, 800, 1100, 1300, and 1500, respectively.

of the phonon modes except the mode at the $\Gamma$ point becomes smaller accompanying the development of structural regularity.

Figure 5 shows the temperature dependence of the electrical conductivity of the samples at various HTT's. The conductivity of the non-HT sample is estimated at 0.76 $\mathrm{S\,m^{-1}}$ at room temperature. With successive heat treatments at intervals of ~200 °C for HTT$\lesssim$600 °C, the conductivity at room temperature shows a drastic increase of four orders of magnitude. In the HTT range $\lesssim$600 °C, the electrical conductivity exhibits obviously semiconductorlike behavior. In this range, the conductivity is explained not by the ordinary thermal activation process, but by the variable-range hopping (VRH) conduction process, which is modified depending on HTT. Figure 6(a) shows the $\log_{10}\sigma$ vs $T^{-1/4}$ plots for the non-HT and HTT 200 samples. Both samples exhibit a linear relation in the $\log_{10}\sigma$ vs $T^{-1/4}$ plots. In contrast, in the HTT region 400–600 °C, the conductivity obeys a linear relation in the $\log_{10}\sigma$ vs $T^{-1/2}$ plots as shown in Fig. 6(b). In the case of HTT 800, the conductivity is not represented by both the thermal activation and the hopping conduction in spite of a 300% decrease in the conductivity upon a temperature change from room temperature to 4.2 K. There is a change in the trend of the conductivity between the low and high HTT ranges, which borders around HTT 800–1100 °C. This indicates the presence of an insulator-metal transition, around HTT 800–1100 °C, although the change is not discontinuous, different from that observed in the ordinary metal-insulator transition. For the samples heat treated above 1100 °C, the conductivity shows only a weak temperature dependence with a slight positive slope in the $\log\sigma$ vs $T$ plot. In addition, a small drop in the conductivity appears at low temperatures below ca. 20 K, which becomes less obvious with the elevation of HTT.

Figure 7(a) shows the temperature dependence of the thermoelectric power of the samples at various HTT's. Because of the high resistivity, the data for HTT 200 could be obtained only in the temperature range above 200 K. All of the samples except HTT 200 exhibit very small thermoelectric powers in the range of 0–1 $\mu\mathrm{V\,K^{-1}}$ in contrast with other disordered carbon systems ($\gtrsim$10 $\mu\mathrm{V\,K^{-1}}$).[1] The thermoelectric power of HTT 200 is an order of magnitude larger than that of other samples as shown in Fig. 7(a). The samples with HTT 400, 800, 1300, and 1500 show a similar temperature dependence and absolute values, suggesting weak HTT dependence. In the temperature range above 100 K, the thermoelectric power has a linear relation with temperature, while in the region T<100 K, it tends to diverge as the temperature decreases as shown in Fig. 7(b). All of the samples have positive thermoelectric power in the whole temperature region except HTT 1300.

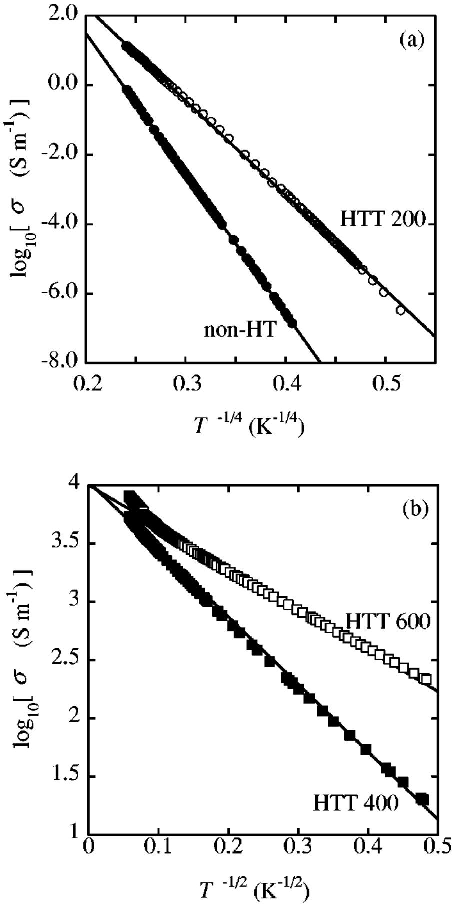

FIG. 6. (a) The $\log_{10}\sigma$ vs $T^{-1/4}$ plot for non-HT (solid circles) and HTT 200 (open circles). (b) The $\log_{10}\sigma$ vs $T^{-1/2}$ plot for HTT 400 (solid squares) and HTT 600 (open squares). Solid lines are the least-squares fits with linear lines. In the high-temperature region, a deviation from the linear relation appears, because the VRH model becomes inappropriate.

## IV. DISCUSSION

Here, we discuss the electronic structure and electron transport properties of the disordered carbon in relation to the heat-treatment-induced structural change on the basis of the experimental results obtained. From the structural characterization, a structural change is suggested to take place

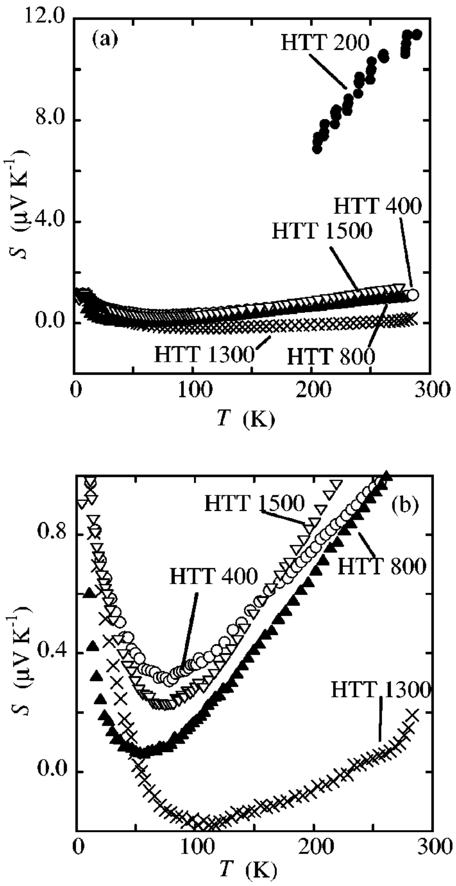

FIG. 7. (a) The temperature dependence of the thermoelectric power of the samples at various HTT's. Solid circles, open circles, solid triangles, crosses, and open triangles denote HTT 200, 400, 800, 1300, and 1500, respectively. (b) The details in the temperature dependence of the thermoelectric power for 400 °C$\leqq$HTT$\leqq$1500 °C. The symbols are the same to those in (a).

around HTT 500 from nongraphitic disordered structure with atomic-scale randomness to graphite-domain-based disordered structure. This change in the structure induced by heat treatment affects the electronic structure and transport properties.

Actually, even the non-HT sample has almost 90% of $sp^2$-carbon atoms, as suggested by the EELS measurement. The rest minority $sp^3$ sites act as defects and induce strains to the $sp^2$ network, resulting in the deformation of graphitic structure, in which the $\pi$-electron network develops. Then, the electronic structure in the non-HT sample is expected to be far from that of graphite. The development of the graphitic structure through the heat-treatment-induced migration of the $sp^3$ defects tends to extend the $\pi$-conjugated areas at the expense of strain energy. As a result, the developed $\pi$ band comes to fill the $\sigma$-$\sigma^*$ gap, and the density of the states around the Fermi level increases as HTT increases. In the higher HTT region (HTT$\gtrsim$1300 °C), where the conversion of $sp^3$ carbon to $sp^2$ carbon can start, the electronic structure of the samples is expected to approach that of bulk regular graphite, though it is modulated by remaining defects.

The electron transport process is affected by the structural change as well. Indeed, as shown in Fig. 5, the conductivity increases accompanied with an insulator-metal transition around HTT ~1000 °C as HTT is elevated. The strong random potential produced by defects is considered to make the electronic states localized, resulting in the insulating feature in the conductivity in the low HTT region. A sharp increase of the conductivity upon heat treatment in the low HTT insulating region (HTT$\lesssim$800 °C) is attributed to the consequence of the structural relaxation from a nonequilibrium state. In the insulating region, there is a crossover in the conductivity behavior around HTT 200–400 °C, below and above which $\log_{10}\sigma$ obeys a linear relation with $T^{-1/4}$ and $T^{-1/2}$, respectively. This suggests that the electron transport process is governed by the 3D variable-range hopping process at low HTT's below the crossover point, whereas the carrier correlation plays an important role above the crossover point. The increase in the density of states and the enhancement in the structural regularity induced by heat treatment elevate the carrier density and the mean free path in the conduction process, respectively, resulting in an enhancment of the conductivity of the samples. According to theory with consideration of the carrier correlation,[29] the conductivity of the samples is described as

$$\sigma=\sigma_0\exp\left[-\left(\frac{T_0}{T}\right)^{1/2}\right], \tag{4}$$

$$T_0=\frac{6e^2}{\pi k_{\mathrm{B}}}\frac{1}{4\pi\epsilon}\frac{1}{\xi}, \tag{5}$$

where $\sigma_0$, $\epsilon$, and $\xi$ are the conductivity at $T=\infty$, the permittivity representing the screening effects on the charges at metallic islands, and the localization length of the wave function, respectively. The carrier correlation generates a gap (Coulomb gap) around the Fermi energy, which is calculated as $k_{\mathrm{B}}e^4D_0\xi/\epsilon$, where $D_0$ represents the electronic density of states at the Fermi energy. The contribution of the Coulomb gap to the conduction becomes effective when the thermal energy is enough smaller than the gap width. Then, the Coulomb gap is at work in the temperature region lower than the characteristic temperature represented as

$$T_{\mathrm{c}}=\frac{e^4D_0}{\epsilon^2}\xi. \tag{6}$$

Therefore, the crossover in the conductivity is explained in the following way. The characteristic temperature is proportional to the localization length. In the non-HT and HTT 200 samples, the ordinary 3D variable-range hopping feature proves that the localization length $\xi$ is considerably shrunk, which is consistent with the presence of atomic-scale disorders. In contrast, the conductivity satisfying the Coulomb-gap variable-range hopping (CGVRH) model indicates a steep increase in $\xi$ in HTT 400 and HTT 600.

Here, from Eq. (5) with the observed conductivity, the localization length is estimated for the samples in the insulating state with the assumption of $\epsilon=10$, which is usually adapted for disordered carbon materials,[30] as shown in Fig. 3. The localization length increases as HTT is elevated, as suggested above. For the HTT 800 sample, $\xi$ is considerably large in comparison with that for the samples with HTT $\lesssim 600\,^\circ\mathrm{C}$ although the estimated value of $\xi$ is unrealistically large due to the limited applicability of the CGVRH formula in HTT 800. It should be noted that a large difference between the localization length and the in-plane lattice domain size $L_a$ is present as shown in Fig. 3, where the value of $\xi$ has to be treated semiquantitatively for HTT 800. The large localization length spans over 20 and 200 graphitic domains at the HTT 600 and 800 samples, respectively. The HTT 400 sample has still a large $\xi$, although graphitic structural features are absent in the XRD profile. In general, the localization length of the electron system does not always correspond to the characteristic length of lattice regularity. In other words, the wave function can be extended in a wide range over the characteristic length if the random potential generated by defects or lattice irregularity is small enough. For example, in the case of the electron transport of carbon nanotubes with defects, the electron can be transported between the electrodes without any scattering in the resonance condition, although the structural regularity is broken by defects between the electrodes. This result of the present sample evidences that metallic conduction does not always need graphitic structure of an extended $\pi$-electron system in carbon material. Therefore, coherent electron transport over the characteristic length of lattice regularity appearing in the present samples strongly indicates that the presence of graphitic structure is not requisite for metallic carbon.

In the second place, the change in the electron conduction for $800\,^\circ\mathrm{C} < \mathrm{HTT} < 1100\,^\circ\mathrm{C}$ is discussed, where the samples are in the vicinity of the insulator-metal transition. The extremely large localization length of HTT 800 and the weak temperature dependence of the conductivity are attributed to the metallic nature in the conduction in spite of the positive slope in the $\sigma$ vs $T$ plot. The insulator-metal transition at HTT 800–1100 can be explained in terms of the following mechanism. Though the graphitic domain size is still within $\sim 3$ nm for the HTT 1100 samples from the XRD results, the fusion between the graphitic domains induced by heat treatment starts generating an infinite percolation path network of metallic grains in the whole system. Eventually, this results in the formation of electronic coherence in the macroscopic scale and gives metallic character in the samples heat treated at high temperatures. It is suggested that the dc conductivity is sensitive to the global feature in the percolation network rather than the feature of the local structures, which is contrasted to the behavior of thermoelectric power as will be discussed later.

In the region $\mathrm{HTT} \gtrsim 1100\,^\circ\mathrm{C}$, the samples have a metallic conduction nature, in which the electronic structure model based on 2D graphene can work judging from the obtained structural information. According to the Drude model for the 2D graphene $\pi$ band, the conductivity of the metallic state is represented by the following formula:

$$\sigma = \frac{ne^2\tau}{m^*} = \frac{ne^2 v_\mathrm{F}\tau}{\hbar k_\mathrm{F}} = \frac{e^2}{\pi\hbar I_c} k_\mathrm{F}\tilde{l}, \tag{7}$$

where $\tau$, $m^*$, $n$, $v_F$, $k_F$, and $\tilde{l}$ are the relaxation time of the carriers, the effective mass of the carriers, the carrier density, the Fermi velocity, the Fermi wave number, and the mean free path, respectively. Equation (7) suggests that $\sigma$ is subjected to the $k_\mathrm{F}\tilde{l}$ value. In other words, we can estimate the value of $k_\mathrm{F}\tilde{l}$ from the observed conductivity. Figure 8 shows the HTT dependence of the $k_\mathrm{F}\tilde{l}$ values, which are obtained from the room-temperature conductivity given in Fig. 5 for $800 \lesssim \mathrm{HTT} \lesssim 1500\,^\circ\mathrm{C}$. Phenomenologically, the condition, whether metallic conduction is achieved or not, is described as $k_\mathrm{F}\tilde{l} > 1$ (metal) or $k_\mathrm{F}\tilde{l} < 1$ (insulator). In all the HTT region, the samples have considerably smaller values of $k_\mathrm{F}\tilde{l}$ than 1, being suggested to be far from metallic electronic states. However, in the application of the model of 2D graphene electronic structure, it is necessary to consider that the actual conductivity is explained in terms of a combination of in-plane and interplane carrier transport processes of graphitic domain in the sample. A large anisotropy in the conductivity between a well conductive inplane process and a less conductive inter-plane process is expected to reduce the conductivity to some extent, in comparison with that calculated on the basis of the in-plane transport band model. Thus, the actual conductivity is represented by multiplying Eq. (7) by the aspect ratio factor of the samples. However, in the present material, the XRD results suggest that graphene sheets strongly prefer an orientation parallel to the current direction, and the correction for the aspect ratio cannot give even an order of magnitude increase in the value of $k_F\tilde{l}$. As a result, in the viewpoint of the in-plane transport contribution, the samples with $\mathrm{HTT} > 800$–$1100\,^\circ\mathrm{C}$ are thought to be in the region $k_\mathrm{F}\tilde{l} \lesssim 1$, where the electronic structure of the system is seriously affected by randomness, and both metallic and insulating domains are distributed in space, which is evidenced by the feature of thermoelectric power as we will discuss next. The value of $k_F\tilde{l}$ shows a steep increase at HTT 1500, which implies that the development of graphitic regions is accelerated through $sp^2/sp^3$ conversion above that HTT.

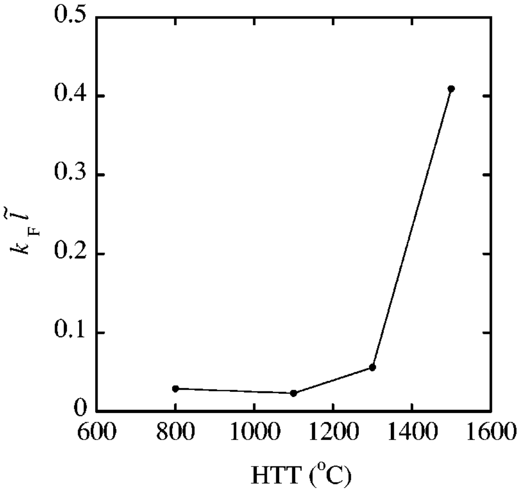

FIG. 8. The $k_\mathrm{F}\tilde{l}$ value obtained from the room-temperature conductivity shown in Fig. 5 for $800 \leqq \mathrm{HTT} \leqq 1500\,^\circ\mathrm{C}$.

The thermoelectric power also gives information on the electronic structure in relation to the structural change.

Though the measured thermoelectric power is limited within a narrow high-temperature region for the HTT 200 sample having atomic-scale disorder, there is a critical difference in the absolute values between HTT 200 and HTT$\gtrsim$400 °C. HTT 200 exhibits a large thermoelectric power over 10 $\mu$V K$^{-1}$ at room temperature, while the others have an order of magnitude smaller values, which are almost in the same range ($\sim$1 $\mu$V K$^{-1}$ at room temperature) irrespective of HTT. It should be noted that the value of the thermoelectric power, $\sim$1 $\mu$V K$^{-1}$, is more than one order of magnitude smaller than that for ordinary graphitic disordered carbon systems. Taking into account that atomic-scale $sp^2/sp^3$ disorder is converted to random network of $sp^2/\pi$ electron domains around 400 °C$<$HTT$<$600 °C, the change in the thermoelectric power is considered to be caused by such a structural change taking place in that HTT range. Then, it is worth comparing the behavior of the thermoelectric power with that of the dc conductivity near the insulator-metal transition. As shown in Fig. 5, the dc conductivity shows a drastic change associated with the development of the infinite percolation path network in the vicinity of the insulator-metal transition. On the other hand, the thermoelectric power does not exhibit any appreciable change around HTT $\sim$1100 °C. This can be explained by taking the spatial inhomogeneity of the sample into consideration. In the case of systems where both metallic and insulating domains are randomly distributed in space, the thermoelectric power is given by the sum of the contributions from both domains.[31] such systems, the contribution of insulating domains makes the thermoelectric power diverge at low temperatures, while the metallic domains give linear temperature-dependent thermoelectric power (diffusion term) at high temperatures. Thus, the thermoelectric power is roughly described as follows:

$$S \sim \frac{E_a}{eT} \quad \text{(at low temperature)}, \tag{8}$$

$$S \sim \frac{\pi^2 k_B^2 T}{3eE_F} \quad \text{(at high temperature)}, \tag{9}$$

where $E_a$ and $E_F$ are the activation energy (corresponding to the band gap) in the insulating domain and the Fermi energy in the metallic domains, respectively. The thermoelectric power observed is well explained by the combination of the insulating and metallic domains given in Eqs. (8) and (9) for HTT $\gtrsim$400. Using Eqs. (8) and (9) with the observed thermoelectric powers, $E_a$ are estimated as 0.0090, 0.0071, 0.018, and 0.011 eV for HTT 400, 800, 1300, and 1500, respectively. $E_F$ are also obtained as 0.47, 5.9, 4.9, 15, and 3.7 eV for HTT 200, 400, 800, 1300, and 1500, respectively. Now, we focus on the behavior of the high-temperature region, where the metallic domains dominate the thermoelectric power. The observed positive thermoelectric power suggests the conduction dominated by hole carriers for all samples. However, if the thermoelectric power model derived from the diffusion term for a single type of hole carriers is simply adapted, the estimated values 5.9–15 eV of the Fermi energy are unrealistically large for graphitic systems especially for 400$\lesssim$HTT$\lesssim$1500, since they are larger than the in-plane transfer integral ($\gamma_0 \sim$ 3 eV).[32] The apparently large values are consistently interpreted by the coexistence of carriers having opposite charges as discussed in the following way. In the actual samples, there coexist metallic and insulating domains with various sizes and structures, as suggested above. Moreover, it is the natural consequence that the Fermi levels are distributed depending on domains as well as the energy gaps in the insulating domains. This leads to spatial fluctuations in the positions of the Fermi levels even in the assumption of similar electronic structure for each domain, as schematically shown in Fig. 9. The density of states is given by

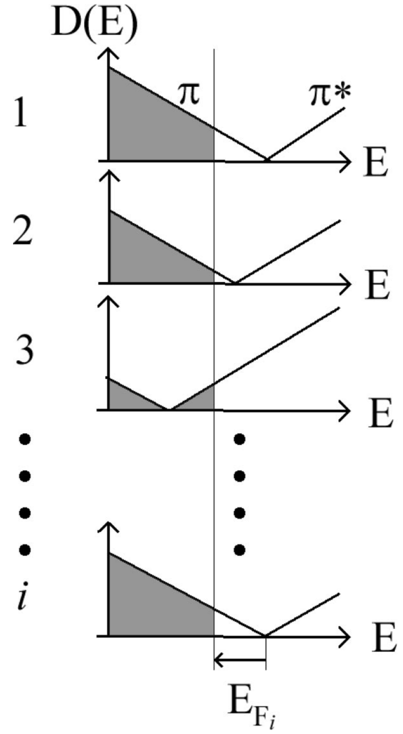

FIG. 9. Schematic model of the distribution of the Fermi levels in the assembly of metallic domains. $D(E)$ is the density of states. 1,2,3, . . . ,$i$ denote domains. The vertical solid line represents the location of the Fermi level of the whole system. The Fermi level of each domain is measured with respect to the contact point of the $\pi$ and $\pi^*$ bands. Domains having contact points above (below) the Fermi level of the whole system have holes (electrons).

$$D(E) = \frac{8}{3\pi} \frac{1}{\gamma_0^2 a^2} |E| \tag{10}$$

for the case where the Fermi energy is located at the contact point between the $\pi$ and $\pi^*$ bands. Here $a$ is the in-plane lattice constant of graphite, and $E<0$ and $E>0$ for the valence $\pi$ band and conduction $\pi^*$ band, respectively. In the present disordered carbon, each metallic domain is positively or negatively charged up through mutual charge transfer so as to achieve consistency with the net remaining charge, which is related to the mean Fermi energy in the whole system. In other words, the mutual charge transfer works to make the positions of the contact points randomly distributed in the metallic domains. A similar charge-transfer effect associated with the difference in the electron affinities between tubes having different diameters in multiwall carbon nanotubes is also reported.[33] Eventually, both domains with hole carriers and electron carriers can coexist in the present systems, where carrier concentrations vary depending on domains. In the whole system, the compensation of hole and electron carriers gives extremely small positive thermoelectric power as observed in the experiments. The positive thermoelectric power observed can be understood on the basis of two possible reasons. One is the presence of defects with $\sigma$ character ($\sigma$ trap),[34,35] the charge transfer to which generates vacancies in the $\pi$ bands, the hole carriers being slightly superior to the electron carriers. The other is the presence of functional groups having electrically negative atoms such as oxygen, which also induce charge transfer from the $\pi$-conjugated systems.

Then, we discuss the appropriateness of the above consideration by the following a simple model. Here, we focus only on the metallic domains, where the graphite linear band structure [Eq. (10)] is assumed for each metallic domain. The distribution of the Fermi levels of metallic domains $E_{\mathrm{F}_i}$ shown in Fig. 9 is assumed to obey the Gaussian distribution $P(E_{\mathrm{F}_i})$,

$$P(E_{\mathrm{F}_i})=\frac{1}{\sqrt{2\langle(\Delta E_{\mathrm{F}})^2\rangle\pi}}\exp\left[-\frac{(E_{\mathrm{F}_i}-\langle E_{\mathrm{F}}\rangle)^2}{2\langle(\Delta E_{\mathrm{F}})^2\rangle}\right], \qquad (11)$$

with the center fixed at the mean Fermi energy of the whole system $\langle E_{\mathrm{F}}\rangle$:

$$\langle E_{\mathrm{F}}\rangle=\sum_i E_{\mathrm{F}_i}P(E_{\mathrm{F}_i}). \qquad (12)$$

Thus, the total thermoelectric power $S$ is denoted as

$$S=\sum_i \frac{\pi^2 k_{\mathrm{B}}^2}{3eE_{\mathrm{F}_i}}P(E_{\mathrm{F}_i})T, \qquad (13)$$

where $k_{\mathrm{B}}$ is the Boltzman constant. Using Eqs. (11)–(13), the deviation of the distribution $\sqrt{\langle(\Delta E_{\mathrm{F}})^2\rangle}$ can be estimated from the observed thermoelectric power. In order to avoid the divergence of the thermoelectric power at the degeneracy point ($E_{\mathrm{F}}=0$) of the linear bands in the calculation, the energy region with a width of $\sim 0.01$ eV is excluded at the contact point.

We employ two possible values as the mean Fermi energy, $\langle E_{\mathrm{F}}\rangle=0.1$ and 0.01 eV, taking into account that the Fermi energy of graphite varies mainly by changing the interlayer resonance integral whose value is estimated at $\gamma_1\sim 0.39$ eV in bulk regular graphite. From the numerical calculation, the observed thermoelectric power (for example, $S\sim 0.8\ \mu\mathrm{V\,K}^{-1}$ at 200 K for HTT 1500) gives deviations $\sqrt{\langle(\Delta E_{\mathrm{F}})^2\rangle}=0.25$ and 0.8 eV in the cases of $\langle E_{\mathrm{F}}\rangle=0.01$ and 0.1 eV, respectively. From this analysis, it is found that the deviations are about one order of magnitude larger than the mean value of the Fermi energy. Consequently, the wide distribution of the Fermi levels among metallic domains in comparison with the mean Fermi energy, which is caused by strong structural randomness, brings about the electron-hole carrier compensation. That results in a considerably small thermoelectric power. From the estimated $\sqrt{\langle(\Delta E_{\mathrm{F}})^2\rangle}$, the deviation of the charge distribution between the metallic domains is calculated as $\sqrt{\langle(\Delta f_c)^2\rangle}\sim 0.01$ per C atom. The inhomogeneous charge distribution gives an additional contribution ($\sim 30\ \mathrm{cm}^{-1}$) to the width of the Raman $G$ band, since electron-hole doping gives a negative-positive shift in the $G$ band. The observed linewidth of the $G$ band ($\sim 100\ \mathrm{cm}^{-1}$; see Fig. 4) might involve the contribution from the inhomogeneity in the charge distribution.

In the case of HTT 200, though the graphitic band structure already becomes nonadoptable, its more defective nature than higher HTT samples makes the hole carriers dominant, where defects induce the charge transfer from the band contributing to the conduction to localized defect states, giving a large thermoelectric power as observed.

## V. CONCLUSION

The heat-treated effect on the electronic properties is investigated for nongraphitic $sp^2$-rich disordered carbon systems with an $sp^2/sp^3$ ratio of ca. 9 in relation to the heat-treatment-induced structural change. The non-HT sample is featured with atomic-scale disorder, whose structure is in a nonequilibrium state far from a thermodynamically stable state. That easily becomes relaxed to disordered graphitic $sp^2$-domain network defined well thermodynamically by heat treatment at considerably low temperatures 200–400 °C. In the high HTT region (HTT$\gtrsim$1300 °C), the structural ordering accompanied by the conversion of $sp^3$carbon into $sp^2$ carbon proceeds toward graphite.

The structural change associated with the formation of graphitic structure clearly affects the electronic and electron transport properties. The structural relaxation in the nonequilibrium region remarkably enhances the electrical conductivity. The change from atomic-scale disorder to the $sp^2$-based graphitic granular system with short-range structural order makes a wide gap of $\sigma$ bands suppressed with the generation of $\pi$ states around the Fermi level. This results in a change in the hopping conduction mechanism at low temperatures in the insulating region because of the increasing importance of the carrier correlation effect in the conduction process. The localization length larger than the in-plane lattice domain size $L_a$ spanning over ten graphitic domains evidences that metallic conduction does not always need graphitic structure of extended $\pi$-electron systems in carbon material.

Above the range HTT 400–600 °C, where the metallic and insulating $sp^2$ domains randomly varying in space coexist, the strong structural randomness causes the remarkably large distribution of Fermi energies among metallic domains, where the deviation is over one order of magnitude upon than the mean Fermi energy. This is the consequence of the mutual charge transfer between domains driven by the spatial fluctuation of the electron affinities. The inhomogeneous charge fluctuations produce domains having electrons and holes. Consequently, the carrier compensation suppresses thermoelectric power, giving a small positive thermoelectric power from the remaining net hole contribution.

The growth of the percolation path network of metallic domains upon heat treatment brings metallic conduction above the percolation threshold (HTT∼1100 °C), where the electronic structure is seriously affected by randomness. The presence of randomness results in a negative slope in the conductivity versus temperature curve even in the metallic region. In contrast, the thermoelectric power is insensitive to the development of the infinite percolation path network, since both metallic and insulating domains in the systems give even contributions, different from the conductivity governed by metallic domains.

## ACKNOWLEDGMENTS

The authors are sincerely grateful to Dr. M. Yudasaka for helpful advice on the sample preparation technique. They also would like to express their thanks to Professor K. Sugihara for fruitful discussions. XRD measurements of the sample were performed at the High Energy Accelerator Research Organization-Photon Factory, and the authors are sincerely grateful to Professor Y. Murakami and Dr. H. Nakao for their great support. The Raman scattering experiments were performed with the support of Professor K. Iio and his students. The present work was supported by a Grant-in-Aid for ''Research for the Future Program,'' Nano-carbons, and Grant-in-aid for Scientific Research No. 13440208 and No. 15105005 from JSPS.

---

*Electronic address: ktakai@chem.titech.ac.jp

†Present address: Japan Space Utilization Promotion Center (Space Experiment Promotion Department), 3-30-16 Nishiwaseda, Shinjyuku-ku, Tokyo 169-0705, Japan.

‡Present address: Matsushita Electric Industrial Co., Ltd., Advanced Technology Research Laboratories 3-4 Hikaridai, Seika-cho, Soraku-gun, Kyoto, 619-0237, Japan.

[1] M. S. Dresselhaus, G. Dresselhaus, K. Sugihara, I. L. Spain, and H. A. Goldberg, *Graphite Fibers and Filaments* (Springer-Verlag, Berlin, 1988).

[2] J. Robertson, Prog. Solid State Chem. **21**, 199 (1991).

[3] Y. Shibayama, H. Sato, T. Enoki, Xiang-Xin Bi, M. S. Dresselhaus, and M. Endo, J. Phys. Soc. Jpn. **69**, 734 (2000).

[4] Odd E. Andersson, B. L. V. Prasad, H. Sato, T. Enoki, Y. Hishiyama, Y. Kaburagi, M. Yoshikawa, and S. Bandow, Phys. Rev. B **58**, 16 387 (1998).

[5] K. Takai, H. Sato, T. Enoki, N. Yoshida, F. Okino, H. Touhara, and M. Endo, J. Phys. Soc. Jpn. **70**, 175 (2001).

[6] K. Tanaka, S. Yamashita, H. Yamabe, and T. Yamabe, Synth. Met. **17**, 143 (1987).

[7] M. Fujita, K. Wakabayashi, K. Nakada, and K. Kusakabe, J. Phys. Soc. Jpn. **65**, 1920 (1996).

[8] A. A. Voevodin and M. S. Donley, Surf. Coat. Technol. **82**, 199 (1996).

[9] M. P. Siegal, J. C. Barbour, P. N. Provencio, D. R. Tallant, and T. A. Friedmann, Appl. Phys. Lett. **73**, 759 (1998).

[10] P. J. Fallon, V. S. Veerasamy, C. A. Davis, J. Robertson, G. A. J. Amaratunga, W. I. Milne, and J. Koskinen, Phys. Rev. B **48**, 4777 (1993).

[11] V. I. Merkulov, D. H. Lowndes, G. E. Jellison, Jr., A. A. Puretzky, and D. B. Geohegan, Appl. Phys. Lett. **73**, 2591 (1998).

[12] M. P. Siegal, P. N. Provencio, D. R. Tallant, R. L. Simpson, B. Kleinsorge, and W. I. Milne, Appl. Phys. Lett. **76**, 2047 (2000).

[13] A. C. Ferrari, B. Kleinsorge, N. A. Morrison, A. Hart, V. Stolojan, and J. Robertson, J. Appl. Phys. **85**, 7191 (1999).

[14] R. Kalish, Y. Lifshitz, K. Nugent, and S. Prawer, Appl. Phys. Lett. **74**, 2936 (1999).

[15] M. Chhowalla, A. C. Ferrari, J. Robertson, and G. A. J. Amaratunga, Appl. Phys. Lett. **76**, 1419 (2000).

[16] J. P. Sullivan, T. A. Friedmann, and A. G. Baca, J. Electron. Mater. **26**, 1021 (1997).

[17] D. G. McCulloch, E. G. Gerstner, D. R. McKenzie, S. Prawer, and R. Kalish, Phys. Rev. B **52**, 850 (1995).

[18] D. G. McCulloch and S. Prawer, J. Appl. Phys. **78**, 3040 (1995).

[19] D. G. McCulloch, D. R. McKenzie, and S. Prawer, Philos. Mag. B **72**, 1031 (1995).

[20] C. Arena, B. Kleinsorge, J. Robertson, W. I. Milne, and M. E. Welland, J. Appl. Phys. **85**, 1609 (1998).

[21] J. Robertson and E. P. O'Reilly, Phys. Rev. B **35**, 2946 (1987).

[22] N. A. Marks, D. R. McKenzie, B. A. Pailthorpe, M. Bernasconi, and M. Parrinello, Phys. Rev. Lett. **76**, 768 (1996).

[23] R. B. Roberts, Philos. Mag. **36**, 91 (1977).

[24] R. F. Egerton and Z. L. Wang, Ultramicroscopy **32**, 137 (1990).

[25] D. L. Pappas, K. L. Saenger, J. Bruley, W. Krakow, T. Gu, and R. W. Collins, J. Appl. Phys. **71**, 5675 (1992).

[26] T. A. Friedmanna, K. F. McCarty, J. C. Barbour, M. P. Siegal, and Dean C. Dibble, Appl. Phys. Lett. **68**, 1643 (1996).

[27] B. E. Warren, Phys. Rev. **59**, 693 (1941).

[28] H. O. Pierson, *Handbook of Carbon, Graphite, Diamond and Fullerenes* (Noyes Publications, Park Ridge, NJ, 1993), p. 257.

[29] A. L. Efros and B. I. Shklovskii, J. Phys. C **8**, L49 (1975).

[30] A. W. P. Fung, Z. H. Wang, M. S. Dresselhaus, G. Dresselhaus, R. W. Pekala, and M. Endo, Phys. Rev. B **49**, 17 325 (1994).

[31] K. Sugihara (private communication).

[32] B. T. Kelly, *Physics of Graphite* (Applied Science Publishers, London, 1981).

[33] Y. Miyamoto, S. Saito, and D. Tománek, Phys. Rev. B **65**, 041402 (2001).

[34] E. A. Kmetko, J. Chem. Phys. **21**, 2162 (1953).

[35] S. Mrozowski, Phys. Rev. **85**, 609 (1952); **86**, 1056(E) (1952).